ARTICLE   OPEN

Trimmed helicoids: an architectured soft structure yielding soft robots with high precision, large workspace, and compliant interactions

Qinghua Guan[1,2], Francesco Stella[1,3], Cosimo Della Santina[3,4], Jinsong Leng[2 ✉] and Josie Hughes[1 ✉]

The development and use of architectured structures is changing the means by which we design and fabricate soft robots. These materials utilize their topology and geometry to control physical and mechanical structural properties. We propose an architectured structure based on trimmed helicoids that allows for independent regulation of the bending and axial stiffness which facilitates tuneability of the resulting soft robot properties. Leveraging FEA and computational analysis we select a geometry that provides an optimal trade-off between controllability, sensitivity to errors in control, and compliance. By combining these modular trimmed helicoid structures in conjunction with control methods, we demonstrate a meter-scale soft manipulator that shows control precision, large workspace, and compliant interactions with the environment. These properties enable the robot to perform complex tasks that leverage robot-human and robot-environment interactions such as human feeding and collaborative object manipulation.

INTRODUCTION

Driven by bio-inspiration[1], many researchers have departed from the classic rigid-robotics paradigm to embrace the inclusion of compliant materials and structures[2–6]. The elephant trunk is an exemplary embodiment of the vision of soft robotics; absent of bone structure, it can be used for tasks ranging from uprooting trees to delicately plucking individual leaves. Its controllability and workspace are exceedingly high, and the compliance endows elephants with an unrivalled muscular multi-tool on the meter scale[7]. Nature holds many other examples of such large-scale structures which simultaneously offer large range of motions, precision, and compliance including octopus tentacles[8], snake bodies[9], and monkey tails[10].

Notwithstanding the impressive soft robots that seek to imitate these biological examples[11–14], animal performances are still unmatched. This is especially the case for larger-scale systems which come close to or exceed the meter scale, where only a few examples exist, all with limited precision and motion capabilities[15–17].

We seek to overcome this limitation by looking to a recent disruptive innovation in material science: architectured structures[18,19]. Instead of relying on the material properties, architectured structures leverage their geometry to tune their physical properties[20,21]. Different from meta-materials which induce customized properties in a material through internal microstructures or the use of composites, architectured structures exploit spatial heterogeneity of a bulk homogeneous material allowing for low-complexity single material fabrication, yet tuning of a wide range of different physical properties[22–24]. As such, architectured structures have been used for a number of robotic applications including actuators[25,26] and deformable[27,28] or adaptive structures[29]. A notable geometry that shows promise for robotic applications is the helical wave spring structure[30–33]. This architectured structure has been tuned to meet a single objective, such as dimensional constraints[32] or bending force[33]. However, many advantageous properties of a soft robot such as the large workspace, compliance and controllability cannot be solely achieved by tuning a single physical parameter. To achieve fully operational robots with a scale and capabilities /comparable to biological soft structure we require the ability to geometrically tune the first two natural modes of deformation, namely the axial and bending stiffness of the structure.

To achieve this goal, we introduce the first example of an architectured structure that has geometric tuneability of the axial and bending stiffness. The structure is formed from a union of helicoid structures, which then undergo radial trimming along the central axis to create trimmed helicoid (TH) structures (Fig. 1a). The helicoid structures has a surface gradient that reduces with radius. This is determined by a single parameter, the helical angle. This variation in gradient means that the steeper inner material prevents compression, contributing mostly to axial stiffness, whilst the outer lower gradient material prevents bending, contributing more to bending stiffness (Supplementary Fig. 1). By combining this with the trimming process which selectively removes the inner material, thus most impacting the axial stiffness, the TH can be designed for a specific ratio between the bending and axial stiffness, as shown in Fig. 1b. The helicoid surface thickness then provides control of the absolute values of the stiffness. This allows the geometry of TH structures to independently determine the axial and bending stiffness whilst enabling a large, and useful, range of stiffness to be generated. These trimmed helical structures (Fig. 1b) can be combined with tendon-driven actuation to achieve soft robot structures that can show compression, bending, and gripping (Fig. 2b). We propose that by selecting appropriate performance metrics, the stiffness, and hence geometry of TH structures, can be tuned to create soft robots that show a range of motion and compliance which is comparable to compliant biological structures.

[1]CREATE Lab, EPFL, Lausanne, Switzerland. [2]Harbin Institute of Technology, Harbin, China. [3]Department of Cognitive Robotics, Delft University of Technology, Delft, The Netherlands. [4]Institute of Robotics and Mechatronics, German Aerospace Center (DLR), Wessling, Germany. ✉email: lengjs@hit.edu.cn; josie.hughes@epfl.ch
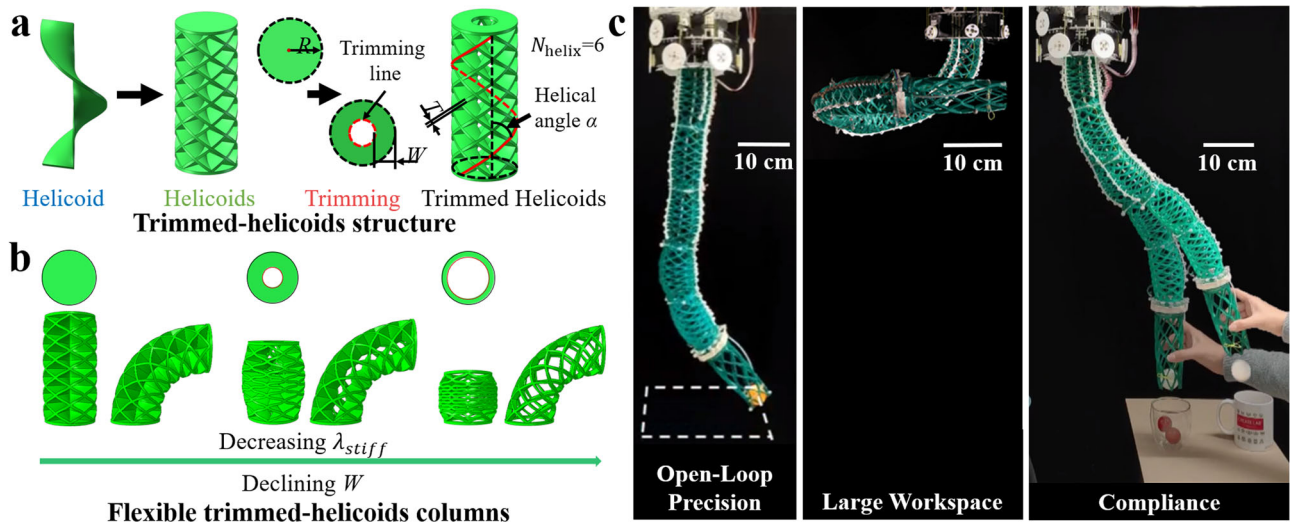
Fig. 1 The concept of a manipulator based on soft architectured structures. a The design of the trimmed-helicoid (TH) structure. T is the thickness of the helicoid, W is the distance from the trimmed edge to the outer radius R, N_{helix} is the helicoid number in one direction, and α is the helical angle of the outer edge of the helicoid. **b** The regulable stiffness ratio $\lambda_{stiff} = K_{axial} R^2/K_{bend}$ of the TH structures by varying the trimming area. K_{axial} and K_{bend} are the axial and bending stiffness, respectively. **c** The high performance of the trimmed-helicoid manipulator on open-loop precision, workspace, and compliance.
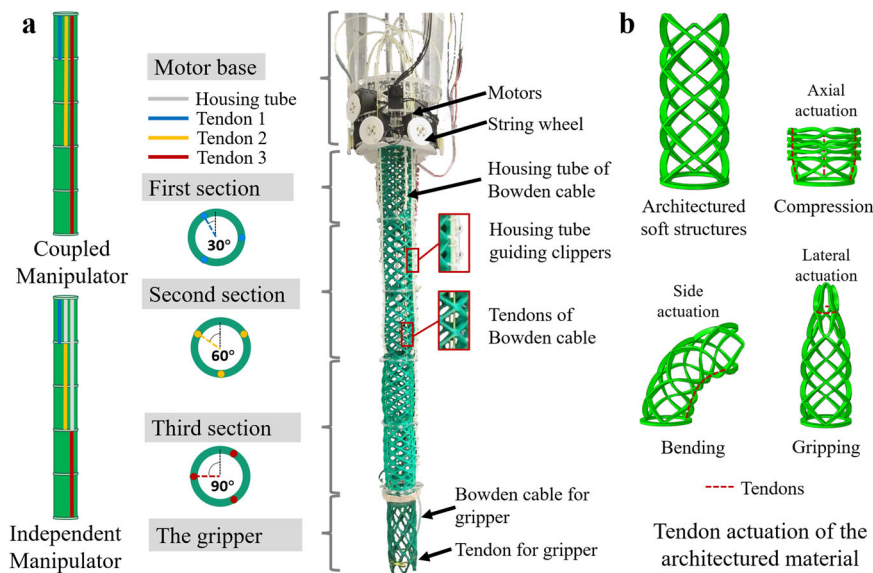

Fig. 2 The tendon-driven manipulator design with Trimmed Helicoids (TH). a The coupled and independent tendon routing (left) and the structure design and tendon routing of the Helix Soft Arm (right). **b** Tendon actuation principles of the TH structure. Via different actuation modes (including axial, side, and lateral actuation), the TH structure can realize contraction, bending and gripping.

Using the TH-based modules as a base structure, we create a tendon-driven 'trunk-scale' soft robotic arm (Fig. 1c). We show that the geometry and hence axial and bending stiffness of the TH structure can be selected to simultaneously influence many key parameters of the soft robot, including sensitivity to control and input noise, compliance, and workspace. Building on this analysis and by optimizing the geometry for given performance requirements, we show the advantages of using trimmed helicoid soft arms for use cases that require precision, compliance, and large workspace. Thanks for these properties, the soft arm can show the necessary dexterity, safety and compliance to be used around humans and exploit environmental interactions. Thus, we show how the soft arm can be used to show the completion of challenging tasks including human feeding and human-assisted object sorting.

RESULTS
Architecture structures display a variety of mechanical properties as a function of their geometry. They allow for low level control of the dynamics of the designed structure and the interactions with the environment[34]. To design robots that leverage trimmed helicoids, it is first necessary to understand how their geometric parameters map to mechanical properties. From here the required mechanical properties can be chosen for a given application based upon how they affect the resulting performance of the robot. In the following we perform this analysis to develop a tendon driven soft robotic arm.

In this section we first characterize the trimmed helicoids, showing the relationship between geometry and the axial and bending stiffness. This is followed by an evaluation of how the stiffness properties act on the performance of a tendon-driven soft

manipulator formed from modular TH units. This includes analysis of the workspace, compliance and robustness to errors in the control inputs. Using this analysis, we select the appropriate geometry of TH structures to create a soft robotic arm with a length of 0.9 m and 9 degrees of actuation (Fig. 2). The resulting control precision and workspace demonstrates how the design analysis enables the robot to have advantageous capacities. Specifically, we highlight how the robot workspace and compliance enable it to perform tasks that require intelligent environmental interactions and safe-human interactions.

Stiffness properties of Trimmed Helicoid architectured structures

For any actuated structure, the bending stiffness and the axial stiffness are two key parameters that drive the resulting workspace, compliance and sensitivity to perturbations[35]. To identify how the design affects these performance parameters, it is first necessary to understand the relationship between geometry and stiffness properties. For architectured structures such as trimmed helicoids these stiffnesses are largely driven by their geometrical parameters; in our case, these are the helicoid thickness T, helicoid width W, helicoid number N_{helix} and helical angle a, as shown in Fig. 1a. To investigate the relationship between the geometric parameters and the axial/bending stiffness, FEM analysis was conducted for different geometries. In this analysis, base geometrical parameters of fourth order relationship with (W/R). We introduce the relative stiffness ratio $\lambda_{stiff} = K_{axial}R_0^2/K_{bend}$ (K_{axial}: axial stiffness, K_{bend}: bending stiffness and R_0: the radius) which provides a single, dimensionless ratio between these two stiffnesses. Using λ_{stiff}, we see it is approximately constant with thickness yet increases with the 3.42 power of W/R. This is a key property of trimmed helicoids as it enables a large range of possible absolute bending stiffnesses whilst the relative stiffness ratio λ_{stiff} can also be varied significantly. They can also be controlled by independent geometric parameters. The axial and bending stiffness ratio λ_{stiff} can be tuned by adjusting the width to radius ratio (W/R) after which the thickness can be tuned to get desired absolute stiffness.

Although varying the helical angle (a) and number (N_{helix}) was also investigated and can be used to vary the stiffness it also introduces undesired behaviours. When the helices angle is high (Supplementary Fig. 2b) compression causes stress concentration and the deformation behaviour becomes nonlinear. Similarly, when the helicoid density becomes high, thin-wall cylinder bucking emerges (Supplementary Fig. 3).

The relative stiffness ratio λ_{stiff} can be adjusted by trimming in a wide range from 1.3 to 14, a significantly larger range than that achievable by homogeneous trimmed materials ($2 < \lambda_{stiff} \leq 4$), with different absolute stiffness properties obtainable by adjusting the thickness of the helicoid. And although $\lambda_{stiff} \approx 2$ is also achievable with thin cylinder of homogeneous material, the buckling phenomena will make it impracticable, which can be avoided with the TH structure. Moreover, the compressibility of TH structure can also be improved much with the decreasing of the stiffness ratio λ_{stiff} (Supplementary Fig. 4b).

Manipulator design

Manipulator design analysis. The Trimmed helicoids allow for bending and axial stiffness to be tuned through geometry. To select the TH geometry for a given application we must identify the stiffness that provides the best performance for the task. By evaluating different performance metrics for varying stiffness of the structure, the optimal stiffness can be identified for the manipulator, which in turn enables the selection of the geometry. The relevant performance metrics for our soft manipulator include workspace, compliance and controllability. Thus, we evaluate how

the stiffness of the architectured material affects the resulting workspace volume and reachability, sensitivity to tendon force and tendon length, and the cartesian compliance of the end effector. These metrics are evaluated for a three-section soft manipulator, with a triangular arrangement of tendons and 9 actuators (Fig. 2). We consider two different modes of tendon actuation, tendons coupled across the adjoining sections or independent tendon routing enabled by bowden cables and vary the stiffness ratio λ_{stiff} of the architectured structure. Although the axial and bending stiffness can both affect the behavior of manipulator, by introducing the non-dimensional load $F_n = F/(K_{bend}/R_0^2)$, the deformation of the manipulator can be fully described by the relative stiffness ratio λ_{stiff} and the non-dimensional load force. For each stiffness and manipulator configurations the metrics are evaluated in simulation, the implementation of which is described in section 'Manipulator analysis'.

Figure 4a–e shows the performance metrics for increasing stiffness ratio λ_{stiff} and for the two different robot configurations. Figure 4a, b reports the workspace volume and average reachability. The workspace volume and average reachability of the coupled manipulator is consistently lower than the independent one across λ_{stiff}. This arises from the inaccessible area (which is also visible in Supplementary Fig. 7) and the reduction in the possible tendon force states due to the coupling of the tendons. The independent tendon routing shows superior performance with an improvement of over 40% for workspace volume, and the possibility to increase the reachability by more than a factor of 60. For both manipulator configurations the manipulator also has a lower workspace at lower stiffness ratios $\lambda_{stiff} = 1$, this rapidly increases and plateaus with an increase of λ_{stiff}, showing little further improvement after $\lambda_{stiff} = 10$. The reachability similarly increases rapidly with λ_{stiff}, however plateaus earlier, showing little further improvement following $\lambda_{stiff} = 5$.

The sensitivity to tendon force (TF) and tendon length (TL) are defined as the change in end effector position for a given change in tendon force or length respectively and are given in Fig. 4c, d. This reflects the sensitivity of the structure to small errors in the control or unmodeled behaviours introduced by the physical structure which we want to minimize. Alongside the sensitivity metrics, the average Cartesian compliance[35] of the end effector is also computed (Fig. 4f-ii). For each of these three metrics the average value across the workspace is found for a range of λ_{stiff} for both the coupled and independent tendon routing configurations and is shown in Fig. 4c–e.

For the sensitivity to tendon force, both configurations show a similar trend with the sensitivity reducing with λ_{stiff}. However, the sensitivity of the independent tendon routing is almost half that of the coupled routing. After $\lambda_{stiff} = 5$ there is minimal further reduction in sensitivity. For the sensitivity to errors in tendon length, although the independent manipulator shows a high sensitivity at very low values of λ_{stiff}, this rapidly reduces, dropping below that of the coupled tendon routing. The sensitivity of the coupled manipulator shows only marginal variation across λ_{stiff}.

The compliance shows a similar trend to the sensitivity to tendon length. For any increase in λ_{stiff} the compliance reduces, initially reducing rapidly, and dropping below that of the coupled manipulator by $\lambda_{stiff} = 4$. For the coupled manipulator, the maximum achievable compliance is lower than the independent routed manipulator.

This analysis demonstrated that the performance of the independent routed manipulator is preferable for almost all performance metrics and values of λ_{stiff}. Thus, we explore how these metrics vary spatially across the workspace for just the independent routed manipulator. In Fig. 5a the reachability of the manipulator with increasing radius and in the z-axis has been computed across the work space and is represented as a point cloud for four values of λ_{stiff} where the origin represents the base

of the manipulator. As the stiffness increases the higher density areas shifts from the bottom of the workspace to the area directly below the base of the manipulator. This spherical area of reachability shows far more useability, and for stiffness of $\lambda_{\text{stiff}} = 2$ the spatial reachability is particularly well distributed.

In Fig. 5b, c the overall sensitivity and compliance is shown for a vertical plane slicing centrally through the workspace of the robot along the XY direction for the values of $\lambda_{\text{stiff}} = 2, 4, 8, 14$. In general, the compliance and the sensitivity to errors in tendon lengths or forces increase radially, with the highest values at the bottom of the workspace. The sensitivity can also be analyzed in other directions of the worsapce. In the Z direction, the sensitivity and compliance both significantly increase with the distance from the z axis (Supplementary Fig. 5). In the XY direction, the sensitivity or compliance within a Z plane shows a stronger reduction with height (Supplementary Fig. 6).

From this analysis it can be seen that although the absolute reach-ability and workspace increase with the ratio λ_{stiff}, while the average compliance and sensitivity decrease with it. Consequently, it is important to select a value that gives a reach-ability that spans a useful area of the workspace and with a sensitivity and compliance that is appropriately distributed. This reachability, sensitivity and compliance analysis across the workspace highlights how the geometry and specifically λ_{stiff} modulates these properties in a coupled manner. This analysis is fundamental for the appropriate selection of the geometrical properties of the TH structure.

Selection of optimal stiffness. From the simulation results, the workspace and reachability are significantly lower and irregularly shaped for the coupled tendon actuation. Its sensitivity to errors in the tendon force is also much higher. Therefore, independent tendon routing was selected. The position control method used for the robot (Supplementary Note 3) utilizes both tendon forces and tendon length so the control performance is affected by both sensitivities. A stiffness in the range of $\lambda_{\text{stiff}} = 10 - 12$ minimizes the sensitivity to tendon force and tendon length, but its compliance is also the lowest. To maximize the workspace, compliance, the stiffness ratio $\lambda_{\text{stiff}} \approx 2$ was selected. The architectured structures were then manufactured with a TPU 3D printing filament with 72D of hardness.

Capabilities of the architectured structure robot

Following the analysis of stiffness, a 3-section and 10-DoF manipulator (9 Dofs for the body and 1 DoF for the gripper) was built. Composed of 6 trimmed helicoid structures, with bowden cables to enable three independently actuated sections, the body of the manipulator spans over 70 cm. To manipulate and interact with the environment, the manipulator was equipped with a gripper based on the trimmed helicoid architectured structure but actuated along the circumference, as depicted in Fig. 2. The helical angle of this gripping section was set as 32.0° to achieve a higher stiffness and larger radius deformation. In this section, the workspace and reachability, control precision and interaction compliance of the robot is demonstrated. The workspace and control precision are first characterized before complex human-robot interaction tasks that require a large workspace, control precision and compliance are shown.

Workspace analysis. Using motion capture the work space of the end effector of the robot can be measured and compared to that from simulations. The workspace range was first verified with a workspace test at the twisting angle of 0°, shown in Fig. 6a(i), b(i). All sections are bent in the same direction and at constant rate until all tendons are contracted by 70 mm, corresponding to the maximum compression strain of 0.5. There is a close match in the predicted and experimental workspace. The reachability of the

manipulator was also evaluated under similar tendon length control but with an offset in bending angle introduced between section such that the manipulator shows different twisting configurations. Figure 6a(ii-iv) &b(ii-iv) shows this for twisting angles of 30°, 90°, 150°. As each section of the manipulator is controlled independently, the manipulator can bend in twist and coil, showing a large accessible area. For the case of 150° offset (Fig. 6a(iv), b(iv)) the manipulators twists around the Z axis below the base of the robot which is challenging for a coupled manipulator to reach. The large work space area and reachability can provide high task compatibility, flexibility of use and easy trajectory planning for the manipulator.

Control precision. To evaluate the control precision, circle, square and null-space trajectories (Mov. S2) are planned for different heights, configurations and offsets within the workspace of the robot. The planned trajectory is compared to experimental motion capture recordings of the robot for a number of repeats (Fig. 7). The implementation of the controller uses linear-strain inverse statics and is discussed in section, 'Manipulator control'. The control precision was evaluated by computing the root mean squared error (RMSE) between the measured and planned trajectories. This is reported in Supplementary Table 1 with the trajectories shown in Fig. 7. The result of the circle trajectories show that with an increase in height, the XY plane precision increases from a RMSE of 3.1 cm to 2.8 cm whilst the Z-axis precision reduces from 1.6 cm to 1.9 cm (Fig. 7a and Supplementary Table 1). This reflects the sensitivity results given in Fig. 4.

The results of the null-space trajectories also verified the relationship between the control precision and sensitivity. The RMSE of the null-space trajectory around the z axis without XY target offset was 2.7 cm (XY) and 1 cm (Z). When an X offset of 0.1 m is introduced, this increased to 3.2 cm (XY)& 2.2 cm(Z), and for 0.1 m Y offset it is 4.7 cm (XY) & 1.6 cm(Z). As previously seen, the Z sensitivity is much lower than the XY sensitivity in the lower area of the workspace, while the overall and XY sensitivity are highest at the extremes of the y-axis.

Different configurations can also affect the trajectory precision, this is particularly highlighted for square trajectories. Due to the high reach-ability of the manipulator, square trajectory could be achieved by the manipulator moving symmetrically around the trajectory, or with a single pose (Mov. S1). However, the symmetrical configuration has better performance in terms of both the RMSE and offset, which could be caused by the varied sensitivity and hysteresis of the structure for different static configurations.

Exploitation of compliance: demonstration tasks. In addition to the precision of the manipulator, the compliance is another key contribution of the architectured structure. The stiffness and hence geometry was selected to enable this compliance whilst maintaining high precision. This compliance allows the manipulator to exploit interactions with the environment, leveraging the body and structure to aid task completion. It also means that the robot is safer around humans with respect to rigid arms, allowing humans to easily interact with the robot. Two demonstrations that exploit the control precision, large workspace and also compliant environment and human interactions are shown. The first is collaborative robot-human tomato picking and sorting (Fig. 8 and Mov. S3).

In the robot-human tomato picking-and-sorting, a trajectory is manually planned for the end effector to transfer soft objects from a bowl on the left to cups on the right. To demonstrate the exploitation of compliance we record the trajectory and motion of the robot with and without external (human and environment) interactions.

The 'interaction-free' trajectory of the end effector is recorded using a motion capture system and is shown in Fig. 8a which

shows a strong correspondence with the planned trajectory. This matching can also be visualized clearly in the top view of the trajectory shown in Fig. 8c. The trajectory is then recorded when the environment and human interaction is introduced. The trajectory is shown in 8b with a visual representation of the task shown in 8d. The manipulator first exploits the interactions with the bowl and the tomato to allow repeated picking of the objects. This interaction with the bowl leads to a difference in the 'picking' part of the interaction between the interaction free, and interaction-based trajectories. Following picking, the manipulator has the precision to accurately move to the cup to place the tomatoes. However, when a different object is picked up, in this case a ping-pong ball, instead of the tomato, the human would intervene and distort the manipulator into another position to place this inclusion in another cup enabling collaborative sorting, as shown in Fig. 8d. The trajectory distortion can be seen in Fig. 8b and Supplementary Movie 3. In this demonstration the task is enabled by compliance. This allows the manipulator to interacting with both the environment (the bowl and objects) and the human, showing the adaptive and safe nature of the robot.

The second more challenging demonstration that uses a larger workspace and exploits the precision and compliance is robot-human fondue serving (Mov. S4). In this task, the robot manipulator picks the fork, forks the bread from a bowl, dip the bread in the fondue pan, and then feeds the bread to human (Fig. 9a). The human participants were allowed to interact with the manipulator to get the bread if required or desired to demonstrate safe human-robot interaction. Figure 9b shows the planned and measured trajectories which highlights how the interaction with the environment enables more complex tasks. The robot first picks the fork exploiting the high precision to reach the desired position and the compliance to accurately align with the fork handle (Fig. 9b, right). After gripping, the fork is then used to pick the bread (Fig. 9b, left). Instead of relying on accurate path planning, the interaction forces arising from the directional Cartesian stiffness of the manipulator is exploited. Following this, the bread is dipped in the fondue pot (Fig. 9b, left) and a movement in the null space is used to move the bread within the cheese. Finally, the bread is moved to the human to complete the feeding task. Here the human can either eat from the robot, or interact safely with the manipulator to move it to the desired position. This human interaction is shown in Fig. 9b (left) and Supplementary Movie 4.

Since the manipulator is very compliant, even with a hard metal fork, participants felt safe to grasp and move the manipulator to feed bread to themselves. The robot-human fondue not only shows its safety around humans but also shows high adaptability to the environment. The perceived safety is also important in allowing the human participants to feel comfortable around the soft arm, despite the potential risk of the sharp fork and hot food. This task is enabled by the precision, compliance and workspace of the arm which results from the advantageous properties of the Trimmed Helicoid architectured structures.

DISCUSSION

In this work we proposed an architectured structure, the trimmed helicoids, and a design methodology that supports design decisions by mapping the high-level performance back to the geometrical properties of the TH structure. Using this approach, we develop a soft manipulator optimized for end-effector compliance, workspace and robustness to errors in control signals. This TH allows for independent selection of axial and bending stiffness which enables this optimization of structure. By developing a model of a general manipulator with variable stiffness properties, we analysed the effect of varying the stiffness ratio λ_{stiff} and tendon routing. The analysis showed how coupled tendon-routing and having a low stiffness ratio λ_{stiff} leads to a workspace

that has a sizeable inaccessible area in the central area. However, introducing a Bowden cable mechanism to achieve independent tendon-routing and increasing λ_{stiff} lead to a dramatic increase in the volume of the workspace and the reachability. The structures actuated with decoupled tendons also showed the lowest sensitivity to control error and also the lowest end-effector compliance at high values of λ_{stiff}. The analysis developed is agnostic of the specific fabrication method, and thus could be used or applied in the development of other robot arms from different architectured structures or actuation methodologies. However, the TH structure allows for direct tuning of the key parameter λ_{stiff} so can directly leverage this analysis.

The realisation of the robot and characterization of the workspace and control precision reinforced that $\lambda_{stiff} = 2$ provides the performance required for many soft manipulation tasks. The reachability and workspace characterization highlighted the superiority that results from manipulators with decoupled tendon actuation. The control precision was investigated by recording different trajectories around the workspace, with the manipulator showing minimal open-loop position error. In particular, given the length of the arm structure, these results show superior performance when compared to many other state-of-the arm soft robotic manipulators, as shown in Table 1. Although some other arm structures show comparable or lower error as a function of the length, this often relies on closed-loop control strategies, learning or data-driven control methods, or is only demonstrated on simpler designs such as a 2D single segment structures.

Additional work could further improve the controllability and workspace of the robot. One effect that was observed is that there were some differences between the first and later repeats of a given trajectory. This hysteresis effect is due to the viscosity of the TPU material and friction in the tendon routing system. Investigating alternative materials or fabrication approaches could reduce the hysteresis and thus further improve the control precision.

The compliance and precision of the manipulator was leveraged in the two robot-human demonstrations, namely the tomato sorting and the fondue cooking experiments. These demonstrated the notable performance of the manipulator in terms of the workspace, control precision and compliance. The interaction with humans (human-intervening sorting and feeding) and the environment (picking tomatoes, balls, forks and forking/dipping bread) required for these tasks showed the safety and passive intelligence provided by the natural compliance of manipulator.The trimmed helicoids show many impressive and exciting capabilities as fundamental building block for soft robots. Future work will explore how to improve the mechanical properties of the TH further to tame the effect of hysteresis. This could be achieved at the hardware level with low-viscosity materials or with model-based and data-driven methods[36] to compensate for these effects. Moreover, considering additional tendon routing patterns in the trimmed helicoids, could significantly increase the design space. This could include introducing twisting tendons, which can be realized by one-directional helicoids with a spiral tendon routing. Finally, embedding sensory feedback in the structure would drastically change the way soft manipulators interact with the environment. Embedding proprioceptive information in the TH would allow for closed loop control of the manipulator. This could be achieved by integrating fluidic sensors[37,38] or IMU sensors[39] into the TH structure. Moreover, equipping the manipulator with light weight soft force sensors would allow a measure of the interaction forces and support the human-robot interactions for tasks including human teaching[40].

Table 1. Precision comparison with other works.

	Method		Data input	Length (cm)	Actuation of each section	Section number	Error (mm)	Error/ Length	Test data
		Control Method							
Li (2021)[45]	Closed-loop & Learning	Q-learning Pretrained with Simulator	Simulator and multi-iteration static points	63.0	3-Dofs of pneumatics	4	23 (200 s)	3.7%	Points to points
You (2017)[46]		Q-learning	Multi-iteration static points	63.0	2-Dofs of pneumatics	4	8 (2D)	1.3%	
Centurelli (2021)[47]	Open-loop & Learning	Artificial Neural Network (ANN)	Static points	20	3 DoFs of pneumatics	1	10.6	5.3%	Trajectory tracking
		Trust Region Policy Optimization (TRPO)	Static points and Dynamic trajectories				3.2	1.6%	
Satheeshbabu (2019)[48]		Reinforce-ment Learning	Static points	31	3-Dofs of pneumatics	1	<29.8	9.6%	Points to points
Chen (2016)[49]		K-nearest- Neighbors Regression (KNNR)	Dynamic trajectories	6.3	2 DoFs of tendon-driven and 1 DoF of screw-driven	1	2.15	3.4%	Trajectory tracking
Marchese (2014)[50]	Closed-loop	PID control	Geometry and captured trajectories	23.0	1 DoFs of pneumatics	6	7.1 (2D)	3.1%	Points to points
Liu (2017)[28]	Open-loop	Static model	Geometry and mechanics	25.5	3-Dofs of tendon-driven	1	3.8-9.5	1.5- 3.7%	Points to points
Our work		Inverse static model based on non-constant strain kinematics	Geometry and mechanics	87.7	3 DoFs of tendon-driven	3	4.8%	4.8%	Trajectory tracking

METHODS

FEM simulation

The FEM simulations (Figs. 3, S2, and S3) were conducted in Abaqus 2021. The material was set to linear isotropic elastic material with Young's modulus of 30 Mpa and Poisson's ratio of 0.45, as measured from real-world experiments on the TPU material. In FEM, the TH structure was perturbed with a static load to generate a set displacement. In the bending test, the rotation displacement was set to deform the structure from 0° to 90°, while the axial compression displacement was set to deform the structure axially from 0 mm to 70 mm. Two mesh types were adopted to ensure an appropriate fidelity of simulation. The helical part of the TH structure was meshed with a C3D10 (a 10-node quadratic tetrahedron) while the connection ring at the two ends of the structure were meshed with a C3D8R (An 8-node linear brick). Considering the trade-off between computing time and accuracy, the element size was set to 1.7 mm. All values in Abaqus were recorded in mm. The axial compression and bending load curves were exported from the FEM simulation. When extreme stresses or buckling phenomena were recorded, the simulation was stopped before reaching the desired displacements. Consequently, the load curve recorded stops at certain compression or bending displacement. To analyze the relation between the geometrical parameters and the stiffness, each of the parameters were varied with respect to a base structure. The parameters in the base TH are: $N_{helix} = 6$, $\alpha = 33.2°$, $H = 10$ mm, $R = 30$ mm, $W = 6$ mm. To evaluate the stiffness curves, each parameter was varied in turn from this base geometry configuration. The parameters varied were the thickness T, width W and angle α of the helix structure, as well as the number of helicoid N_{helix} present in the structure. The parameters were sampled as:

$T = 1, 2, 3, 4, 5$ [mm], $W = 6, 12, 18, 24, 30$ [mm], $\alpha = 52.6°$, $33.2°$, $23.1°$, $18.6°$, $N_{helix} = 3, 6, 9, 12$ The axial stiffness was obtained by the linear fitting of compressing forces with the displacement in a range of 0–21 mm and the bending stiffness was obtained by the linear fitting of bending moments with the bending angle in a range of $0 - 27°$.

Manufacturing process of the architectured structures

The helical structures were 3D printed on a Flashforge Creator Pro2 3D printer with soft TPU (hardness 72D). The printing parameters were set as extruder temperature of 220 °C, layer height 0.18 mm, and printing speed 60 mm/s. The final structure was further optimized with respect to the analytical description of the TH to reduce the stress concentration that occurs at high compression. A sine wave structure was used to smooth the pattern and reduce the stress concentrations, as shown in Fig. 3e. The modified structure shows the same mechanical properties of the helix structure Supplementary Fig. 4, so that the whole analysis holds true.

Manipulator fabrication

The manipulator is formed from six architectured TH structures connected serially with screws to form a 0.9 m long manipulator structure. The first 5 elements act as the body of the manipulator, while the last one is used as gripper. The body of the manipulator is split into three segments. The first 'upper' section consists of one cylinder segment, and the other two sections are composed of two cylindrical segments each, this is illustrated in Fig. 2. The architectured gripper was attached as an additional section to the end of the manipulator.

This manipulator is mounted such that it is hanging from the motor-base which houses 10 motors (Dynamixel, XM430-W210-R) which are stacked in two-layers. In the first lower layer, three motors are directly attached to the tendons in the first section via

20 mm pulleys. A further six motors control the tendons in the second and third section via Bowden cables. In each of the section the cables are equally spaced around the circumference. The final motor is connected via a Bowden cable to the tendon that is routed radially around the tip of the gripper to allow for opening and closing. Compression springs are used to achieve antagonistic action of this gripper.

The Bowden cables allow independent actuation of the different sections. To operate in this manner, they display low friction and enough stiffness to prevent buckling. The Bowden cables are composed of two layers of PTFE pipes (4×2 mm and 2×1 mm tubes) and a 0.8 mm inner nylon string. To control each degree of actuation independently, the housing tube of the Bowden cable starts from the upper base plate, is curved through
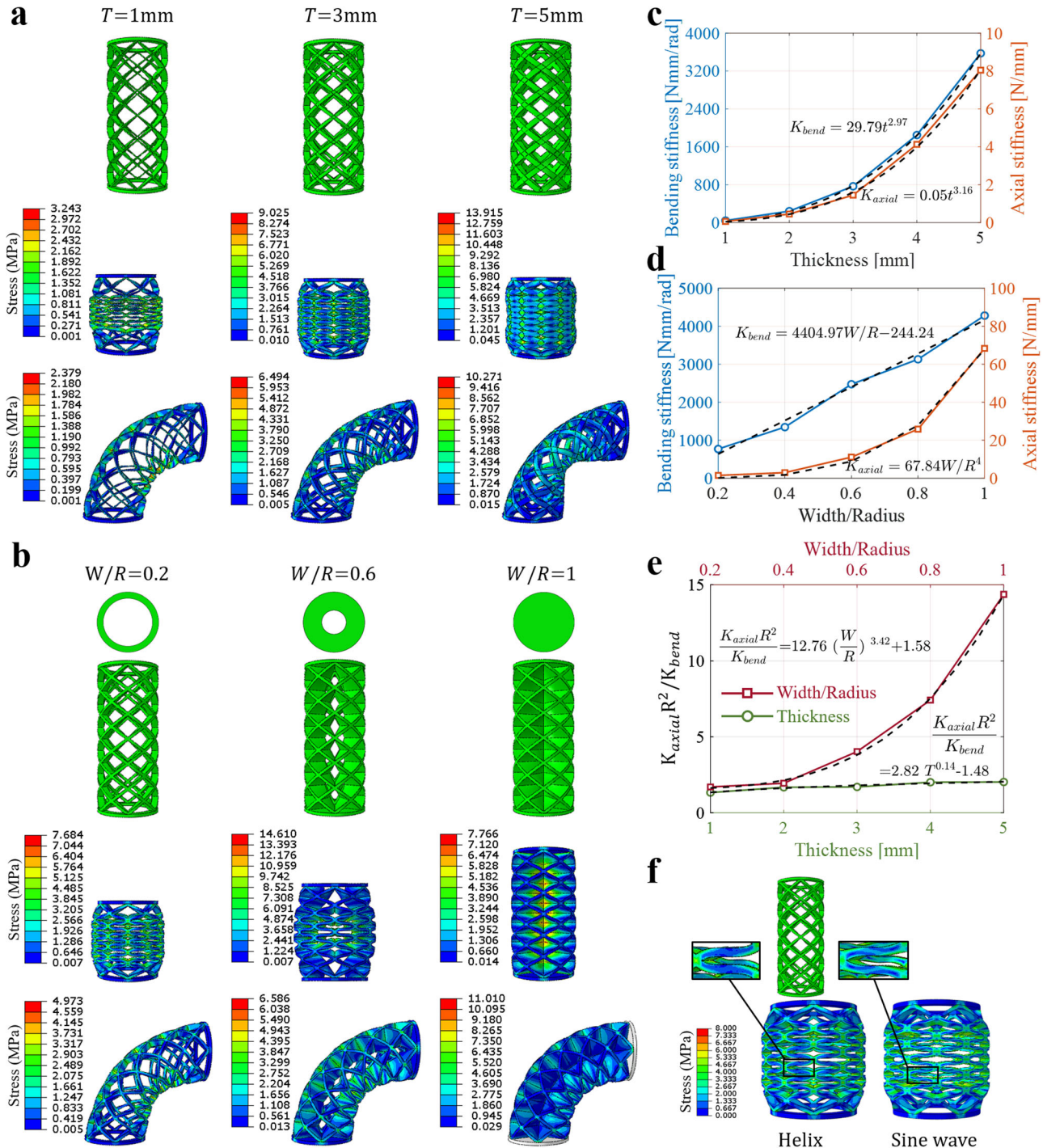
Fig. 3 FEM simulation of TH (Trimmed Helicoids) architectured structures with varied thickness and width. a FEM simulation of TH architectured structures with varied thickness T. **b** FEM simulation of TH architectured structures with varied width W. **c** Axial and bending stiffness of TH architectured structures with varied thickness T. **d** Axial and bending stiffness of TH archi-tectured structures with varied width to radius ratio (W/R). **e** Non-dimensional stiffness ratio $\lambda_{\mathrm{stiff}} = K_{\mathrm{axial}} R^2/K_{\mathrm{bend}}$ of TH architectured structures with varied thickness and width and (**f**) equivalent mapping from the helix structure to the sine wave structure.
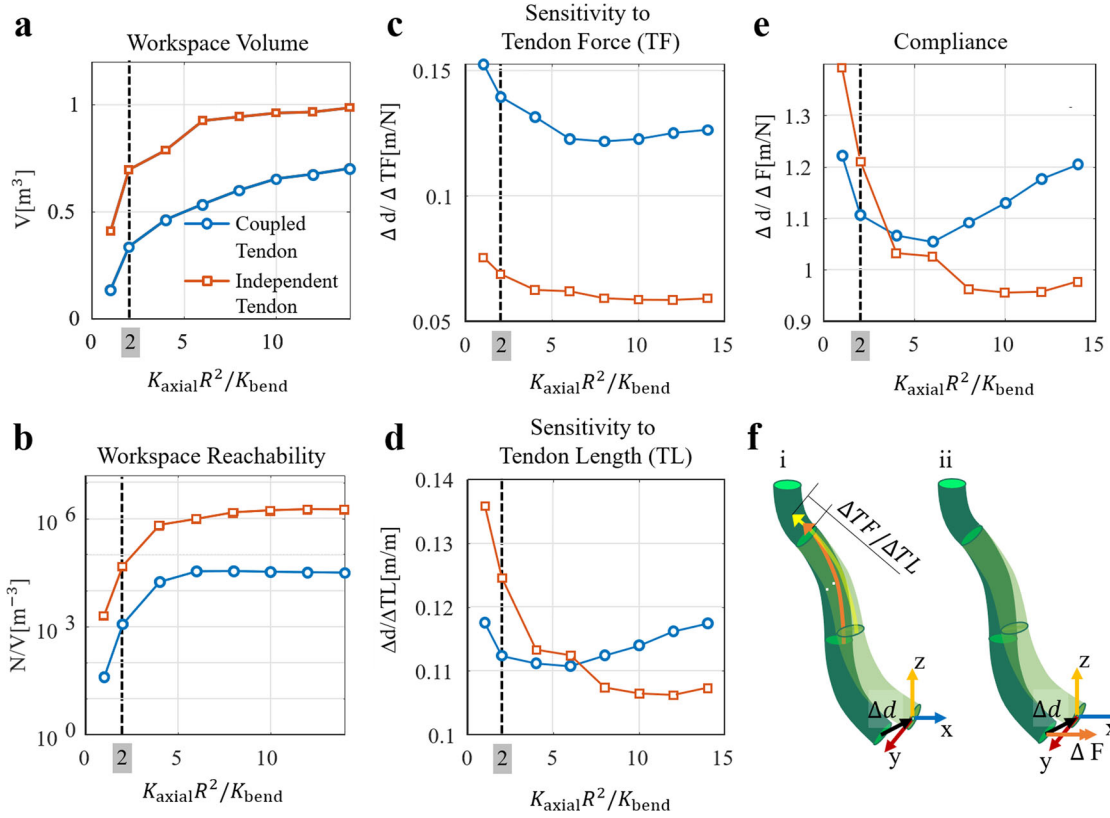
Fig. 4 The sensitivity, compliance, workspace and reach-ability analysis of coupled/independent manipulators with varied stiffness ratio λ_{stiff}. **a** The relationship between the workspace volume to the stiffness ratio λ_{stiff}. **b** The relationship between average reachability to the stiffness ratio λ_{stiff}. **c** The relationship between the averaged sensitivity to tendon force (TF) and the stiffness ratio λ_{stiff}. **d** The relationship between the averaged sensitivity to tendon length (TL) and the stiffness ratio λ_{stiff}. **e** The relationship between the averaged compliance and the stiffness ratio λ_{stiff}. **f** The definition diagrams of Sensitivity and Compliance. (i) $\Delta TF/TL$ is the variation of tendon force/length, and Δd the resulted manipulator end displace variation. (ii) ΔF is the variation of load on the end of the manipulator, and Δd the resulted manipulator end displace variation.

180°, after which is passed through the motor-base and is then guided by the clippers along the manipulator to the start position of the gripper and each section. The inner tendon is then guided in the walls of the architectured cylinder axially (for the body sections) or circularly (for the gripper sections) to ensure the fastening points on the end of each section, as shown in Fig. 2. The Dynamixel motors are controlled from Matlab, leveraging the Dynamixel SDK package.

Manipulator analysis

To perform the analysis of the control sensitivity, compliance and workspace, we developed a linear strain model based on the projection of solution space for a general soft manipulator[41–44], (see in Supplementary Notes 1.1 and 1.2 for more details). The manipulator is modelled as a three-section soft manipulator which has the same lengths and structure as the manipulator that is fabricated (Fig. 2). We consider the two cases of coupled and independent tendon routing. For all the analysis we compute the metrics for stiffness ratios of $\lambda_{stiff} = 1, 2, 4, \ldots, 14$.

The sensitivity to tendon force (TF) or tendon length (TL) is determined in Cartesian space by finding the displacement in the x, y and z axis for a change in tendon force or length, i.e. $\Delta d_i/(\Delta TF/TL)$, $i = x, y, z$ (Fig. 4d). From this, the overall and XY sensitivities are defined as the square root of the sum of squares of all components and the x,y components, respectively. In a similar way, the compliance components are defined as the displacement for a given disturbance force in the x, y, and z axes, i.e. $\Delta d/\Delta F_i$, $i = x, y, z$. The overall and XY compliance can also be found for these.

To obtain the sensitivity of the whole manipulator, the origin transformation matrix T_i of one single section at configuration state i was computed in the three-dimensional actuation space (moments on x and y axes, and the axial force). The varied transformation matrices (Tv^F, Tv^L) were calculated by applying unit perturbations to the tendon force or length $\delta(TF/TL)_j$ to the configuration state i. Thus a state set, $N_1 = \{T_i, Tv^F_{i,j}, Tv^L_{i,j}\}$, $i = 1\ldots N, j = 1\ldots 3$ was obtained, where N is the state number of one single section in the three-dimension actuation space.

Then, the origin (S_i) and varied ($Sv^F_{i,j}$, $Sv^L_{i,j}$) transformation matrices of the whole manipulator in full actuation space (nine-dimension tendon forces) was derived by multiplying by the transformation matrix of each section in a sequence (Eq. 1). Thus, a configuration state set of the whole manipulator, $N_2 = \{S_i, Sv^F_{i,j}, Sv^L_{i,j}\}$, $i = 1\ldots N^3, j = 1\ldots 9$ as obtained, where N^3 is the state number of the manipulator in the full actuation space of nine tendon forces:

$$S_i = S_{k,m,n} = T_k T_m^2 T_n^2,$$

$$Sv^{F/L}_{i,j} = Sv^{F/L}_{j,k,m,n} = \begin{cases} Tv^{F/L}_{k,j} T_m^2 T_n^2 \quad 1 \geq j \geq 3 \\ T_k Tv^{F/L}_{m,j-3} {}^2 Tv_n \quad 4 \geq j \geq 6 \\ T_k T_m^2 Tv^{F/L}_{n,j-6} {}^2 \quad 7 \geq j \geq 9 \end{cases} \quad (1)$$

$$i = (k-1)N^2 + (m-1)N + n, j = 1\ldots 9, k, m, n = 1\ldots N$$

where k,m,n are the state index of each section corresponding to state i in the set of N_3.

In the next step, the tendon forces and tendon lengths were computed based on the tendon routing to check their validation,
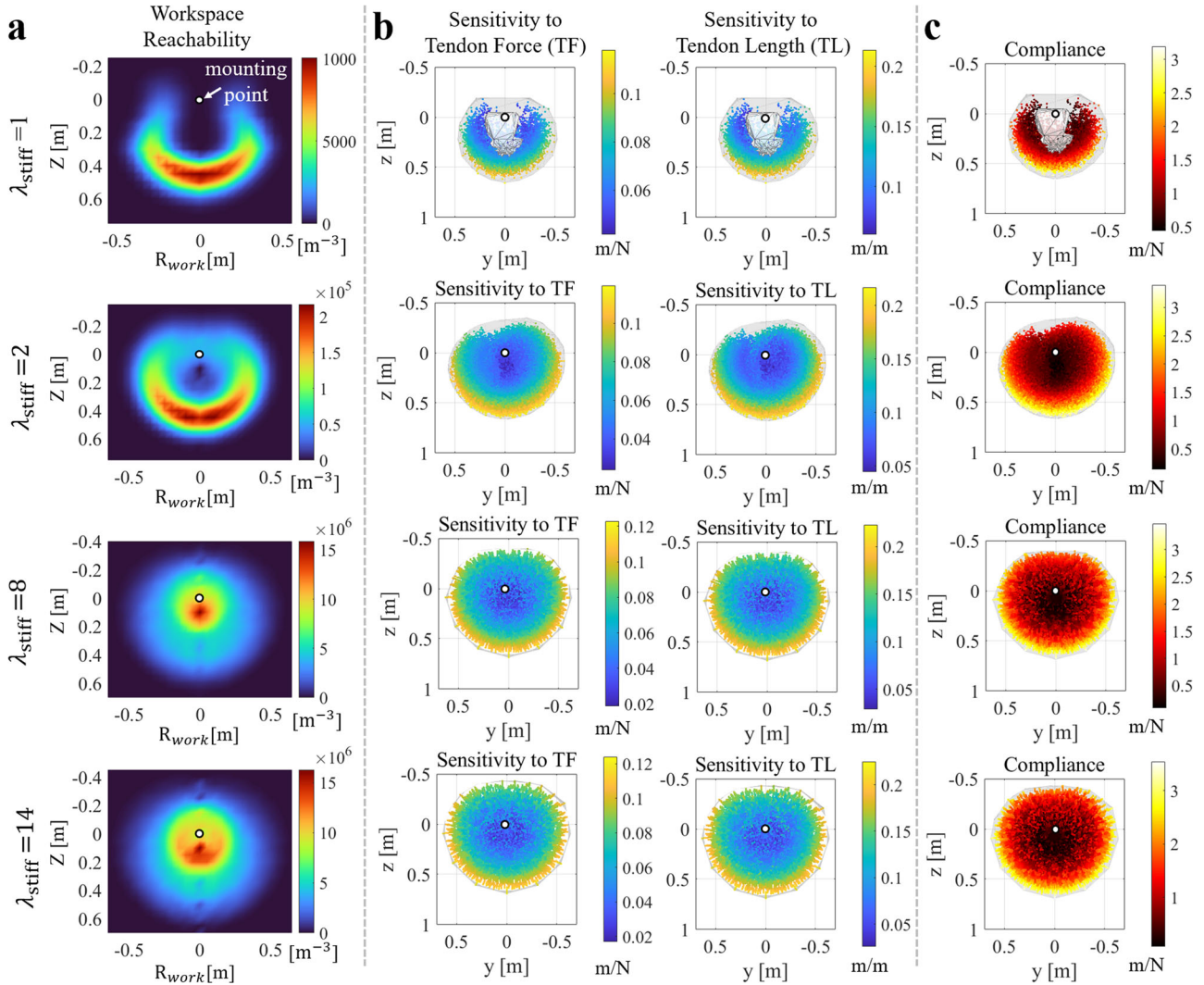
Fig. 5 Overall performance nephograms of the manipulator with the stiffness ratio $\lambda_{\text{stiff}} = 1, 2, 8, 14$ and independent tendon routing. **a** Workspace reachability, **b** sensitivity to Tendon Force (TF) and Tendon Length (TL) and **c** compliance.

and invalid impossible state are excluded to get a valid set of manipulator state $N_3 = \{S_i, Sv_{i,j}^F, Sv_{i,j}^L\}$, $i = 1 \dots M, j = 1 \dots 9$ where M is the valid state number of the whole manipulator. Then the sensitivity matrix of the whole manipulator can then be found from the position variations under the valid state set, N_3, as:

$$S_{i(4\times4)} = \begin{bmatrix} R_i P_{i(3\times1)} \\ 0_{(1\times3)} 0 \end{bmatrix}, \quad Sv_{i,j(4\times4)}^{F/L} = \begin{bmatrix} Rv_{i,j}^{F/L} Pv_{i,j(3\times1)}^{F/L} \\ 0_{(1\times3)} 0 \end{bmatrix},$$

$$Sens_{i(3\times9)}^{TF/TL} = \frac{\delta P_{i,j}^{F/L}}{\delta(TF/TL)_j} = \frac{Pv_{i,j}^{F/L} - P_i}{\delta(TF/TL)_j}, \quad i = 1 \dots M, j = 1 \dots 9 \tag{2}$$

where R_i/P_i and $Rv_{i,j}^{F/L}/Pv_{i,j}^{F/L}$ are the origin and varied rotation matrices or position vectors related to the tendon force or tendon length variation $\delta(TF/TL)_j$ at the state i. $Sens_i^{TF/TL}$ is the sensitivity matrix at state i. Thus, the XY, Z and overall sensitivities of the whole manipulator can be derived from the analysis of one single section, as Eq. 3.

$$Sens_{i,XY}^{TF/TL} = \sqrt{\sum Sens_i^{TF/TL}(m,n)^2}, m = 2, 3, n = 1 \dots 9,$$

$$Sens_{i,Z}^{TF/TL} = \sqrt{\sum Sens_i^{TF/TL}(m,n)^2}, m = 3, n = 1 \dots 9, \tag{3}$$

$$Sens_i^{TF/TL} = \sqrt{\sum Sens_i^{TF/TL}(m,n)^2}, m = 1, 2, 3, n = 1 \dots 9$$

where, $Sens_{i,XY}^{TF/TL}$, $Sens_{i,Z}^{TF/TL}$, $Sens_i^{TF/TL}$ are the sensitivities in XY, Z and overall dimensions respectively.

For the compliance, the origin transformation matrix T_i of one single section at configuration state i was the same to that in the state set of N_1. And varied transformation matrix $(Tv_{i,j}^K)$ of one single segment were calculated by applying unit perturbations on the kinematic parameters $\delta q_{i,j}$, where $q_{i,j}$ is jth component of the general coordinates at the configuration state i, $q_i = [k_{x,i}^0, k_{y,i}^0, \varepsilon_{z,i}^0, k_{x,i}^1, k_{y,i}^1, \varepsilon_{z,i}^1]^T$ (x and y curvatures and elongation ratios at the start and end of the section). Thus a state set of one single section, $N_4 = \{T_i, Tv_{i,j}^K\}$, $i = 1 \dots N, j = 1 \dots 6$ were obtained.

Then, similarly to the sensitivity analysis, the origin (S_i) and varied transformation matrices ($Sv_{i,j}^K$) of the whole manipulator were derived by multiplying the transformation matrix of each section in a sequence under same configuration states of N_3 obtained in the sensitivity analysis. Thus a configuration state set of the whole manipulator, $N_5 = \{S_i, Sv_{i,j}^K\}$, $i = 1 \dots M, j = 1 \dots 18$ can be obtained. In the next step, the generalized stiffness matrix of the manipulator, K_Q^{mnplt} can be derived from the generalized stiffness matrix of the single segment, K_Q, as Eq. 4, where $L_{0,\text{def}}$ is original length of deformable part, K_{bend} is the bending stiffness
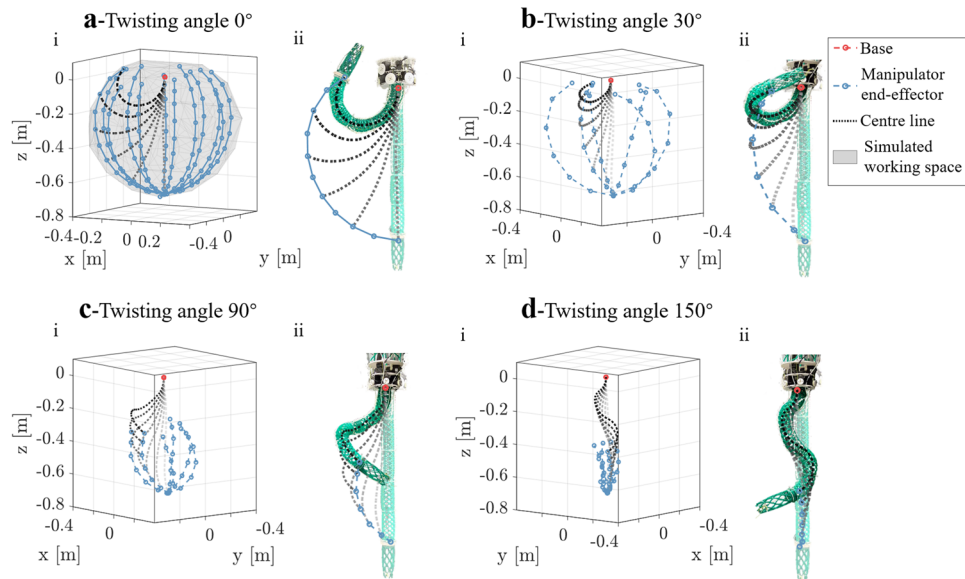
Fig. 6 Workspace (i) and poses (ii) with different twisting angles. a 0°, **b** 30°, **c** 90° and **d** 150°. The simulated workspace envelope of the manipulator is compared with the workspace at the twisting angle of 0° (**a**). The twisting angle is defined as the bending orientation angle offset to the last adjacent section. For example, the twisting angle of 0° means three sections of the manipulator bending in one direction with a constant proportion.
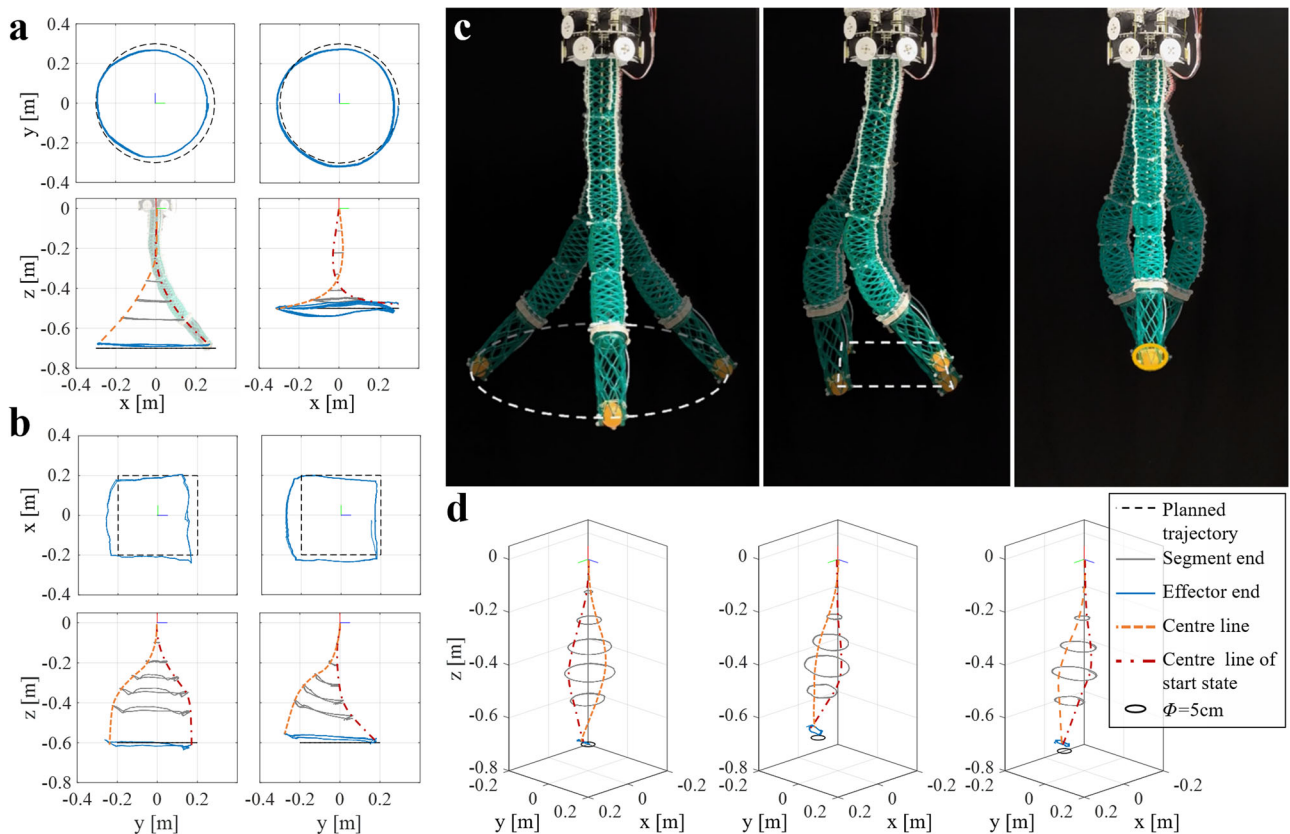

Fig. 7 Trajectory planning results of circles, squares, and null-space. a Circular trajectories of C1 and C2. C1 and C2 were conducted in the heights of 70 cm and 50 cm with the radius of 30 cm respectively. **b** Square trajectories of S1 and S2. S1 and S2 were planned with a same end trajectory in the height of 60 cm and with the edge length of 40 cm, but with symmetrical and mono-directional configurations, separately. **c** The manipulators tracking the circle, square and null-space trajectories. **d** Nullspace trajectories of N1, N2 and N3. N1 was planned tilt to different orientations in a certain angle of 20° at the the position of x = 0 cm, y = 0 cm, z = 70 cm. N2 and N3 were planned at the positions with offsets of y = −10 cm and x = 10 cm with the offset of tilt angles of Rx = −15° and Ry = -15° (counter-clockwise is positive), respectively.
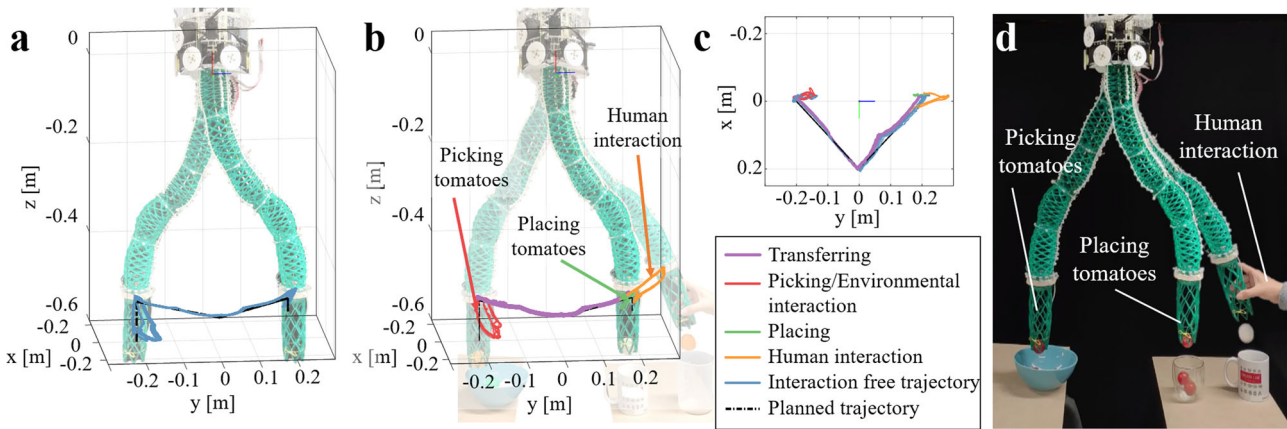
Fig. 8 Robot-human tomato sorting. a Planned and captured trajectories without interaction with environment or human. **b** Planned and captured trajectories with environment and human interactions to pick, place and sort the tomatoes. **c** The top view of the planned, interaction-free and interaction trajectories. **d** The human interacted tomato sorting. Ping-pong balls were picked out by human intervention based on the compliance of the manipulator.
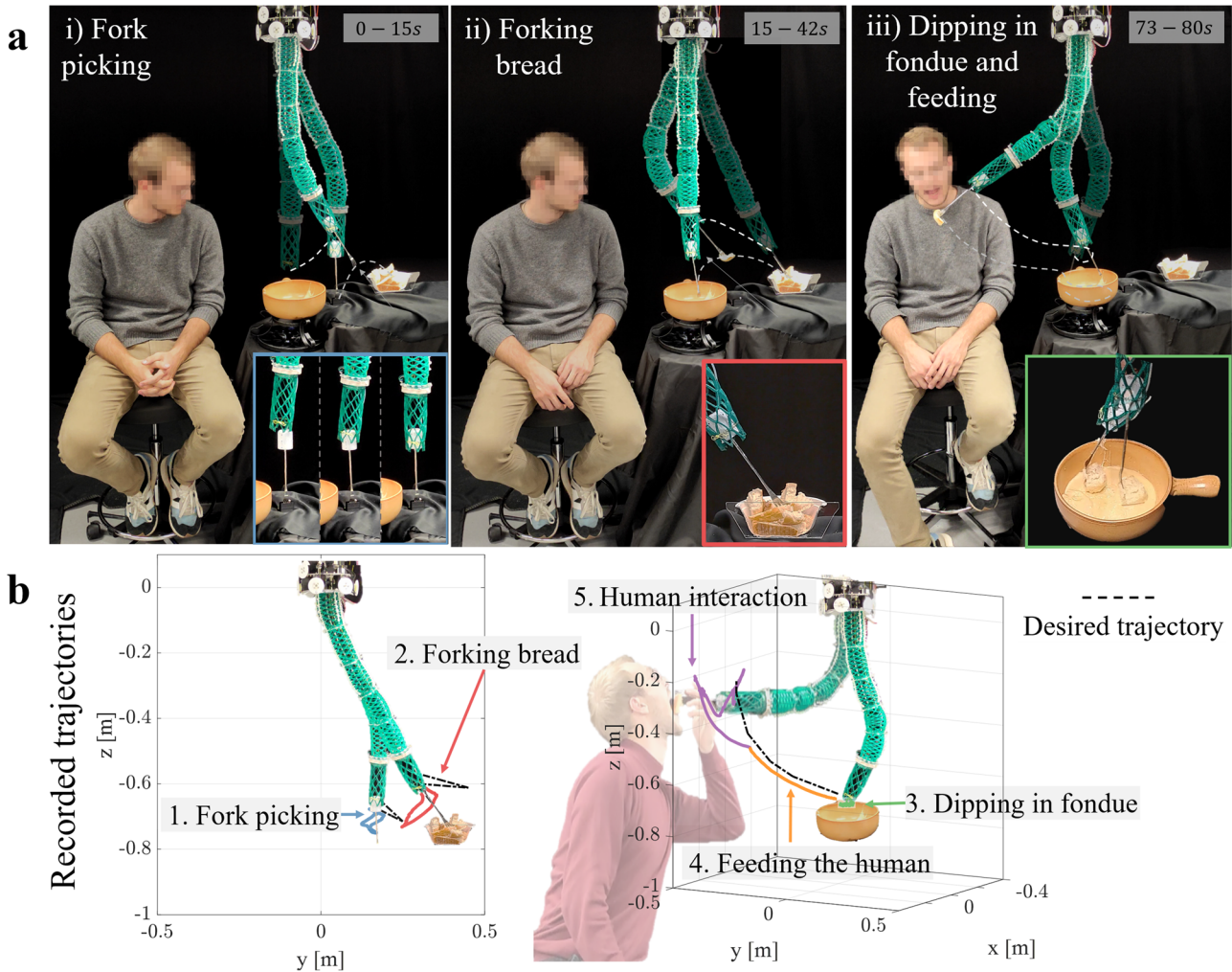

Fig. 9 The Robot-human Fondue. a Real-world pictures of the robot-human fondue experiment, including fork picking(i), forking bread(ii), dipping in fondue and feeding the human(iii). **b** Captured trajectories of the experiment. Notably, thanks to selected compliance, the manipulator is able both to pick objects, as well as comply with external perturbations, being these exerted by the environment (fork, bread, fondue pot) or by the human.

and K_{axial} is the axial stiffness of the helicoid cylinder.

$$K_Q = (L_{0,\text{def}}/6)\text{diag}\left(\begin{bmatrix} K_{\text{bend}} \\ K_{\text{bend}} \\ K_{\text{bend}} \\ K_{\text{bend}} \\ K_{\text{axial}} \\ K_{\text{axial}} \end{bmatrix}\right)\begin{bmatrix} 2 & 1 & 0 & 0 & 0 & 0 \\ 1 & 2 & 0 & 0 & 0 & 0 \\ 0 & 0 & 2 & 1 & 0 & 0 \\ 0 & 0 & 1 & 2 & 0 & 0 \\ 0 & 0 & 0 & 0 & 2 & 1 \\ 0 & 0 & 0 & 0 & 1 & 2 \end{bmatrix}, \quad (4)$$

$$K_Q^{\text{mnplt}} = \begin{bmatrix} K_Q & 0 & 0 \\ 0 & 2K_Q & 0 \\ 0 & 0 & 2K_Q \end{bmatrix}.$$

Then, the Jacobin matrix of the manipulator, $J_{\text{mnplt}}i^K$ at state i can be computed from the origin (P_i) and varied ($Pv_{i,j}^K$) position vectors at the valid state i, as Eq. 5.

$$Sv_{i,j(4\times4)}^K = \begin{bmatrix} Rv_{i,j}^K & Pv_{i,j(1\times3)}^K \\ 0_{(1\times3)} & 0 \end{bmatrix} \quad (5)$$

$$J_{\text{mnplt}i(3\times18)}^K = \frac{\delta P_{i,j}^K}{\delta Q_j} = \frac{Pv_{i,j}^K - P_i}{\delta Q_j}, i = 1\ldots N_3, j = 1\ldots 18.$$

where $Rv_{i,j}^K/Pv^K$ are the varied rotation matrix or position vector related to the kinematic parameter variation δQ_j at the state i, where Q is the kinematic parameter vector of the whole manipulator (Eq. S2). Then the Cartesian compliance matrix of the manipulator at state i can be derived from the intrinsic generalized stiffness matrix K_Q^{mnplt} and the Jacobian matrix $j_{\text{mnplt}i}$, as Eq. 6.

$$Compl_{i(3\times3)} = J_{\text{mnplt}i(3\times18)}^K K_Q^{\text{mnplt}^{-1}} J_{\text{mnplt}i(3\times18)}^{K^\top}, i = 1\ldots N_3 \quad (6)$$

where $Compl_i$ is the compliance matrix at state i. Thus, again, the XY, Z and Overall compliance of the whole manipulator can be derived from the analysis of one single section, as Eq. 7.

$$Compl_{i,XY} = \sqrt{\sum Compl_i(m,n)^2}, m = 2,3, n = 1,2,3,$$

$$Compl_{i,Z} = \sqrt{\sum Compl_i(m,n)^2}, m = 3, n = 1,2,3, \quad (7)$$

$$Compl_{i,\text{Overall}} = \sqrt{\sum Compl_i(m,n)^2}, m = 1,2,3, n = 1,2,3$$

Within this framework, the average reachability shown in Fig. 4b was calculated by sampling each tendon force from 0 to 70 N and calculating the average point density of the end effector position across the workspace.

Motion data collection

The ground truth measurement of the motion of the manipulator was collected using six motion capture cameras (Optic Prime 13) and motion capture markers attached to the join at each cylindrical segment. The markers on each segment were defined as a rigid body in the 'Motive' Software (Optical motion capture software from OptiTrack). The position and attitude information from the markers was collected and exported to Matlab 2021 where the data was post-processed to remove invalid data points, plot and compare the recording against the desired trajectory.

Manipulator control

In this work, we used two methods to control the manipulator. When testing the workspace (Fig. 6), a group of motor sequences was generated to observe the natural motions arising from the equilibrium between the elasticity of the manipulator's structure and the forces exerted by the motors. The actuation space was explored by varying the activation ratio of different groups of motors, as depicted in Fig. 6. For the experiments requiring trajectory planning (Fig. 7) and the human-robot interaction

demonstrations (Figs. 8, 9), an inverse static approach was used. The method computes the tendon actuation needed to achieve the desired trajectory at the gripper's end effector. The planned trajectory includes the position and orientation of the end effector over a set of discrete points to account for the 9 degrees of freedom of the robot arm. The configuration and tendon forces of the manipulator were computed for each discrete point by solving the inverse statics based on a non-constant strain model (see in Supplementary Note 1.3 for more details). Once a statically valid configuration was found, the corresponding tendon lengths could also be derived. Then, the tendon length contraction sequences were converted to the rotation motion sequences for motors. Thus, the PC could send the commands related to these planned trajectories. While solving the static configuration at the target state, the tendon force was set to be higher than zero to prevent the invalid state with slacked tendons, and the maximum strain on the structure was set as -0.5 to avoid over-compression and risk of damage. For the experiments with human participants, written informed consent was provided by all the study participants.

REFERENCES

1. Kim, S., Laschi, C. & Trimmer, B. Soft robotics: a bioinspired evolution in robotics. *Trends Biotechnol.* **31**, 287–294 (2013).
2. Rus, D. & Tolley, M. T. Design, fabrication and control of origami robots. *Nat. Rev. Mater.* **3**, 101–112 (2018).
3. Stella, F. & Hughes, J. The science of soft robot design: A review of motivations, methods and enabling technologies. *Front. Robot. AI* **9**, 1059026 (2022).
4. Della Santina, C. et al. Soft robots. *Encycl Robot.* **489**, 1–15 (2021).
5. Yasa, O. et al. An overview of soft robotics. *Annu. Rev. Control Robot. Auton. Syst.* **6**, 1–29 (2022).
6. Walker, J. et al. Soft robotics: A review of recent developments of pneumatic soft actuators. *Actuators* **9**, 3 (2020). MDPI.
7. Dagenais, P., Hensman, S., Haechler, V. & Milinkovitch, M. C. Elephants evolved strategies reducing the biomechanical complexity of their trunk. *Curr. Biol.* **31**, 4727–4737 (2021).
8. Kier, W. M. & Smith, K. K. Tongues, tentacles and trunks: the biomechanics of movement in muscular-hydrostats. *Zool. J. Linn. Soc.* **83**, 307–324 (1985).
9. Zhang, X., Naughton, N., Parthasarathy, T. & Gazzola, M. Friction modulation in limbless, three-dimensional gaits and heterogeneous terrains. *Nat. Commun.* **12**, 1–8 (2021).
10. Arachchige, D. D. & Godage, I. S. Hybrid soft robots incorporating soft and stiff elements. In *2022 IEEE 5th International Conference on Soft Robotics (RoboSoft)*, 267–272 (IEEE, 2022).
11. Laschi, C. et al. Soft robot arm inspired by the octopus. *Adv. Robot.* **26**, 709–727 (2012).
12. Walker, I. D., Choset, H. & Chirikjian, G. S. Snake-like and continuum robots. In *Springer handbook of robotics*, 481–498 (Springer, 2016).
13. Kolachalama, S. & Lakshmanan, S. Continuum robots for manipulation applications: a survey. *J. Robot.* **2020**, 4187048 (2020).
14. Ben-Tzvi, P. & Liu, Y. Robots with tails. *Mech. Eng.* **143**, 32–37 (2021).
15. Takeichi, M., Suzumori, K., Endo, G. & Nabae, H. Development of a 20-m-long giacometti arm with balloon body based on kinematic model with air resistance. In *2017 IEEE/RSJ International Conference on Intelligent Robots and Systems (IROS)*, 2710–2716 (IEEE, 2017).
16. Li, S. et al. Scaling up soft robotics: a meter-scale, modular, and reconfigurable soft robotic system. *Soft Robot.* **9**, 324–336 (2022).
17. Hawkes, E. W., Blumenschein, L. H., Greer, J. D. & Okamura, A. M. A soft robot that navigates its environment through growth. *Sci. Robot.* **2**, eaan3028 (2017).
18. Shen, S. C.-y & Buehler, M. J. Nature-inspired architected materials using unsupervised deep learning. *Commun. Eng.* **1**, 1–15 (2022).

19. Xia, X., Spadaccini, C. M. & Greer, J. R. Responsive materials architected in space and time. *Nat. Rev. Mater.* **7**, 683–701 (2022).

20. Berger, J., Wadley, H. & McMeeking, R. Mechanical metamaterials at the theoretical limit of isotropic elastic stiffness. *Nature* **543**, 533–537 (2017).

21. Barthelat, F. Architected materials in engineering and biology: fabrication, structure, mechanics and performance. *Int. Mater. Rev.* **60**, 413–430 (2015).

22. Bouaziz, O., Br´echet, Y. & Embury, J. D. Heterogeneous and architectured materials: a possible strategy for design of structural materials. *Adv. Eng. Mater.* **10**, 24–36 (2008).

23. Miyazawa, Y. et al. Heterogeneous origami-architected materials with variable stiffness. *Commun. Mater.* **2**, 110 (2021).

24. Kladovasilakis, N., Tsongas, K., Karalekas, D. & Tzetzis, D. Architected materials for additive manufacturing: A comprehensive review. *Materials* **15**, 5919 (2022).

25. Sedal, A., Fisher, M., Bishop-Moser, J., Wineman, A. & Kota, S. Auxetic sleeves for soft actuators with kinematically varied surfaces. In 2018 IEEE/RSJ International Conference on Intelligent Robots and Systems (IROS), 464–471 (IEEE, 2018).

26. Hasse, A. & Mauser, K. Poisson induced bending actuator for soft robotic systems. *Soft Robot.* **7**, 155–167 (2020).

27. Goswami, D., Liu, S., Pal, A., Silva, L. G. & Martinez, R. V. 3d-architected soft machines with topologically encoded motion. *Adv. Funct. Mater.* **29**, 1808713 (2019).

28. Liu, T., Wang, Y. & Lee, K. Three-dimensional printable origami twisted tower: Design, fabrication, and robot embodiment. *IEEE Robot. Autom. Lett.* **3**, 116–123 (2017).

29. Simons, M. F., Digumarti, K. M., Conn, A. T. & Rossiter, J. Tiled auxetic cylinders for soft robots. In 2019 2nd IEEE International Conference on Soft Robotics (Robo-Soft), 62–67 (IEEE, 2019).

30. Skorina, E. H. & Onal, C. D. Soft hybrid wave spring actuators. *Adv. Intell. Syst.* **2**, 1900097 (2020).

31. Wan, Z. et al. Design, analysis, and real-time simulation of a 3D soft robotic snake. *Soft Robot.* **10**, 258–268 (2022).

32. Salgueiro, J. M. & Reis, J. C. Towards a highly integrated 3D printed soft continuum manipulator. In 2021 7th International Conference on Automation, Robotics and Applications (ICARA) 163–167 (IEEE, 2021).

33. Gunarathna, C. H., Ranasinghe, A. D., Piyumal, N. A., Kulasekera, A. L. & Jayaweera, N. D. Design and characterization of a 3d printed wave spring for use in a flexible robotic arm. In 2022 Moratuwa Engineering Research Conference (MERCon), 1–6 (IEEE, 2022).

34. Mengaldo, G. et al. A concise guide to modelling the physics of embodied intelligence in soft robotics. *Nat. Rev. Phys.* **4**, 595–610 (2022).

35. Stella, F., Hughes, J., Rus, D. & Della Santina, C. Prescribing cartesian stiffness of soft robots by co-optimization of shape and segment-level stiffness. *Soft Robot.* **10**, 701–712 (2023).

36. Jiang, H. et al. A two-level approach for solving the inverse kinematics of an extensible soft arm considering viscoelastic behavior. In 2017 IEEE International Conference on Robotics and Automation (ICRA), 6127–6133 (2017).

37. Vicari, A. et al. Proprioceptive sensing of soft tentacles with model based reconstruction for controller optimization. In 2023 IEEE International Conference on Soft Robotics (RoboSoft), 1–6 (IEEE, 2023).

38. Junge, K. & Hughes, J. Soft sensorized physical twin for harvesting raspberries. In 2022 IEEE 5th International Conference on Soft Robotics (RoboSoft), 601–606 (IEEE, 2022).

39. Hughes, J., Stella, F., Santina, C. D. & Rus, D. Sensing soft robot shape using imus: An experimental investigation. In International Symposium on Experimental Robotics, 543–552 (Springer, 2021).

40. Liu, W. et al. Touchless interactive teaching of soft robots through flexible bimodal sensory interfaces. *Nat. Commun.* **13**, 1–14 (2022).

41. Stella, F., Guan, Q., Della Santina, C. & Hughes, J. Piecewise affine curvature model: a reduced-order model for soft robot-environment interaction beyond pcc. In 2023 IEEE International Conference on Soft Robotics (RoboSoft), 1–7 (IEEE, 2023).

42. Stella, F., Obayashi, N., Della Santina, C. & Hughes, J. An experimental validation of the polynomial curvature model: identification and optimal control of a soft underwater tentacle. *IEEE Robot. Autom. Lett.* **7**, 11410–11417 (2022).

43. Renda, F., Boyer, F., Dias, J. & Seneviratne, L. Discrete cosserat approach for multisection soft manipulator dynamics. *IEEE Trans. Robot.* **34**, 1518–1533 (2018).

44. Guan, Q., Sun, J., Liu, Y., Wereley, N. M. & Leng, J. Novel bending and helical extensile/contractile pneumatic artificial muscles inspired by elephant trunk. *Soft Robot.* **7**, 597–614 (2020).

45. Li, P. et al. A q-learning control method for a soft robotic arm utilizing training data from a rough simulator. In 2021 IEEE International Conference on Robotics and Biomimetics (ROBIO), 839–845 (IEEE, 2021).

46. You, X. et al. Model-free control for soft manipulators based on reinforcement learning. In 2017 IEEE/RSJ International Conference on Intelligent Robots and Systems (IROS), 2909–2915 (IEEE, 2017).

47. Centurelli, A., Rizzo, A., Tolu, S. & Falotico, E. Open-loop model-free dynamic control of a soft manipulator for tracking tasks. In 2021 20th International Conference on Advanced Robotics (ICAR), 128–133 (IEEE, 2021).

48. Satheeshbabu, S., Uppalapati, N. K., Chowdhary, G. & Krishnan, G. Open loop position control of soft continuum arm using deep reinforcement learning. In 2019 International Conference on Robotics and Automation (ICRA), 5133–5139 (IEEE, 2019).

49. Chen, J. & Lau, H. Y. Learning the inverse kinematics of tendon-driven soft manipulators with k-nearest neighbors regression and gaussian mixture regression. In 2016 2nd International Conference on Control, Automation and Robotics (ICCAR), 103–107 (IEEE, 2016).

50. Marchese, A. D., Komorowski, K., Onal, C. D. & Rus, D. Design and control of a soft and continuously deformable 2D robotic manipulation system. In 2014 IEEE international conference on robotics and automation (ICRA), 2189–2196 (Ieee, 2014).

ACKNOWLEDGEMENTS

AUTHOR CONTRIBUTIONS
J.H. and Q.G. conceived the idea. Q.G. designed and fabricated the architectured structure. Q.G. and F.S. designed and built the manipulator. Q.G. and F.S. designed and conducted all the experiments. F.S. and Q.G. developed the modeling and controlling methods of the manipulator. J.H., Q.G., F.S., and C.S. analyzed the data and wrote the paper. J.L. and C.S. gave constructive advice for this work. J.L. and J.H. directed, supervised and fully revised the research. All authors reviewed the paper.

COMPETING INTERESTS
The authors declare no competing interests.

ADDITIONAL INFORMATION
Supplementary information The online version contains supplementary material available at https://doi.org/10.1038/s44182-023-00004-7.

Correspondence and requests for materials should be addressed to Jinsong Leng or Josie Hughes.

Reprints and permission information is available at http://www.nature.com/reprints

Publisher's note Springer Nature remains neutral with regard to jurisdictional claims in published maps and institutional affiliations.